frontiers in Chemistry

ORIGINAL RESEARCH
published: 13 December 2021
doi: 10.3389/fchem.2021.804204

Construction of UiO-66/$Bi_4O_5Br_2$ Type-II Heterojunction to Boost Charge Transfer for Promoting Photocatalytic CO_2 Reduction Performance

Dongsheng Li[1], *Bichen Zhu*[1], *Zhongti Sun*[1], *Qinqin Liu*[1], *Lele Wang*[1] *and Hua Tang*[2]*

[1]School of Materials Science and Engineering, Jiangsu University, Zhenjiang, China, [2]School of Environmental Science and Engineering, Qingdao University, Qingdao, China

One of the basic challenges of CO_2 photoreduction is to develop efficient photocatalysts, and the construction of heterostructure photocatalysts with intimate interfaces is an effective strategy to enhance interfacial charge transfer for realizing high photocatalytic activity. Herein, a novel UiO-66/$Bi_4O_5Br_2$ heterostructure photocatalyst was constructed by depositing UiO-66 nanoparticles with octahedral morphology over the $Bi_4O_5Br_2$ nanoflowers assembled from the $Bi_4O_5Br_2$ nanosheets *via* an electrostatic self-assembly method. A tight contact interface and a built-in electric field were formed between the UiO-66 and the $Bi_4O_5Br_2$, which was conducive to the photo-electrons transfer from the $Bi_4O_5Br_2$ to the UiO-66 and the formation of a type-II heterojunction with highly efficient charge separation. As a result, the UiO-66/$Bi_4O_5Br_2$ exhibited improved photocatalytic CO_2 reduction performance with a CO generation rate of 8.35 μmol h^{-1} g^{-1} without using any sacrificial agents or noble co-catalysts. This work illustrates an applicable tactic to develop potent photocatalysts for clean energy conversion.

Keywords: UiO-66, $Bi_4O_5Br_2$, photocatalytic, CO_2 reduction, type-II heterojunction

OPEN ACCESS

Edited by:
Tingjiang Yan,
Qufu Normal University, China

Reviewed by:
Yanhui Ao,
Hohai University, China
Huogen Yu,
Wuhan University of Technology, China

***Correspondence:**
Hua Tang
huatang79@163.com

Specialty section:
This article was submitted to Catalysis and Photocatalysis, a section of the journal Frontiers in Chemistry

Received: *29 October 2021*
Accepted: *15 November 2021*
Published: *13 December 2021*

Citation:
Li D, Zhu B, Sun Z, Liu Q, Wang L and Tang H (2021) Construction of UiO-66/$Bi_4O_5Br_2$ Type-II Heterojunction to Boost Charge Transfer for Promoting Photocatalytic CO_2 Reduction Performance. Front. Chem. 9:804204. doi: 10.3389/fchem.2021.804204

1 INTRODUCTION

The high-speed increase of carbon dioxide (CO_2) concentration in the atmosphere has led to serious global warming and environmental problems (Scott and Geden, 2018; Prasad et al., 2020; Tang et al., 2020; Xu et al., 2020; Liu et al., 2021a). Investigating reliable strategies which can convert CO_2 into usable fuel can guide the healthy development of society. Among the numerous proposals for CO_2 conversion, solar photocatalysis that can efficiently convert CO_2 into useful chemical intermediates and chemical raw material (carbon monoxide, CO) has been appraised as a potential strategy that can overcome global warming as well as meet the demand for renewable fuels (Shen et al., 2019; Liu et al., 2020a). Therefore, the development of highly efficient photocatalysts plays a considerable role in the future practical application of photocatalytic CO_2 conversion (Liu, 2016; Wu et al., 2019; Wang et al., 2021a; Wang et al., 2021b).

In recent years, metal-organic framework (MOF) based semiconductors demonstrating attractive characteristics such as high surface area and a well-defined and adjustable porous structure are considered as a promising material for photocatalytic applications of organic pollutants degradation, O_2 production, H_2 production, N_2 fixation, and CO_2 reduction (Hirakawa et al., 2016; Ling et al., 2018; Dong et al., 2019; Mukhopadhyay et al., 2021; Peña-Velasco et al., 2021). Among the assorted

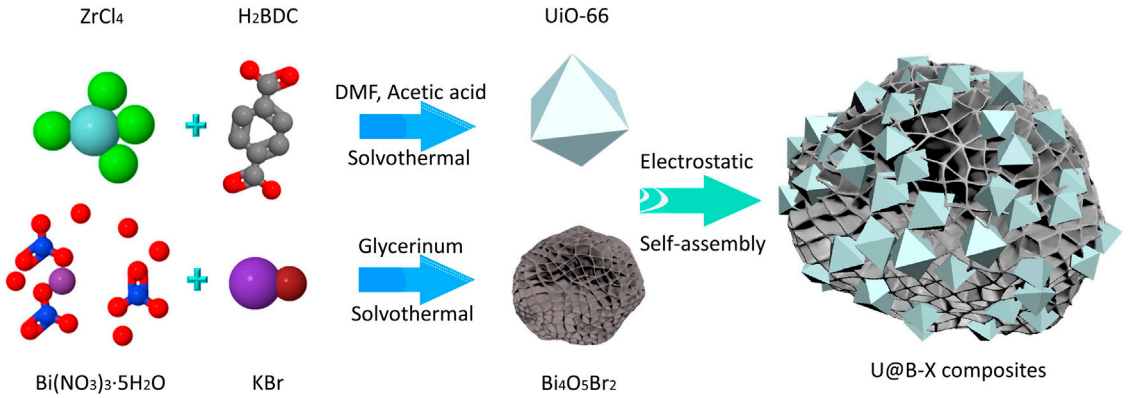

Scheme 1 | Schematic depiction of preparation of U@B-X composites.

MOF-based photocatalysts, UiO-66 is a classic Zr-based MOF material, and it has high thermal stability, unsaturated open metal sites, hygroscopic CO_2 binding sites, and superior CO_2 adsorption capacity. Therefore, UiO-66 is considered a promising candidate for application in photocatalytic CO_2 reduction (Kim et al., 2015; Wang et al., 2018a). For example, Yamani et al. prepared UiO-66-NH_2 based frameworks using a hydrothermal method and found it presented photocatalytic CO_2 reduction activity with the products of CO, CH_4, and $HCOO^-$ (Zeama et al., 2020). However, the pure UiO-66 usually demonstrates a fast recombination rate of electron holes and poor photocatalytic CO_2 reduction activity (Peng et al., 2020). Recently, some tactics, such as replacing the original ligands (Zhang et al., 2021), depositing precious metals or other co-catalysts on the surface (Zhang et al., 2020), and doping other metal elements to form new coordination bonds (Yang et al., 2017) have been investigated to ameliorate the performance of UiO-66. Coupling UiO-66 with another photocatalytic semiconductor to construct a heterostructure composite can adjust the electronic transfer path and achieve high separation efficiency of photogenerated charges, which has been deemed as one of the most promising procedures to elevate the photocatalytic performance (Su et al., 2017).

Choosing a suitable semiconductor is one of the key points to construct heterojunctions with UiO-66. Among the reported semiconductors, bismuth oxyhalide BiOX (X = Cl, Br, and I) consisting of a $[Bi_2O_2]$ layer interlaced by double layers of halogen atoms is a typical layered semiconductor, and it illustrates unique advantages of being chemically stable, non-toxic, and corrosion-resistant (Jin et al., 2019; Ren et al., 2020). It is noted that the band energy structure of BiOX can be controlled by adjusting the Bi content in bismuth oxybromide material. For instance, Ye et al. have fabricated the $Bi_4O_5Br_2$ nanoflowers via a bismuth-rich strategy and found that $Bi_4O_5Br_2$ nanoflowers with high Bi ratio owned smaller band gap and better CO_2 photoreduction activity compared to BiOBr (Ye et al., 2016). Accordingly, the BiOX with adjustable band structure seems to be a promising choice to match with UiO-66 to construct heterojunction photocatalysts for the application of CO_2 reduction.

In this study, a novel UiO-66/$Bi_4O_5Br_2$ (U@B) heterojunction was fabricated *via* an electrical self-assembly method by wrapping the UiO-66 nanoparticles over the $Bi_4O_5Br_2$ nanoflowers (**Scheme 1**). The tight contact interface and matched energy band structure between UiO-66 and $Bi_4O_5Br_2$ could accelerate the charge separation to promote CO_2 reduction property. The UiO-66@$Bi_4O_5Br_2$ hybrid can effectively produce CO at a rate of 8.35 μmol h^{-1} g^{-1} under full-spectrum light irradiation without using any noble co-catalysts or sacrificial agents. This tactic of constructing MOFs-based heterojunction provides a new way to design efficient photocatalysts with CO_2 reduction activity.

2 EXPERIMENTAL

2.1 Fabrication of the UiO-66/$Bi_4O_5Br_2$ Composite

For the preparation of pure UiO-66, 1.0 mmol $ZrCl_4$ (233.04 mg) and 1.0 mmol terephthalic acid (H_2BDC 166.13 mg) were dispersed into 25 ml DMF solution and sonicated for 10 min, respectively. After that, 3.6 ml acetic acid was mixed into the above solution in a 100 ml Teflon-lined autoclave and sonicated for 10 min and then heated at 120°C for 24 h. After that, the collection was centrifugated, washed, and dried overnight at 60°C to obtain the UiO-66. For the $Bi_4O_5Br_2$, 2 mmol KBr, and 2 mmol $Bi(NO_3)_3·5H_2O$ were dispersed into 20 ml glycerol and stirred for 10 min, respectively. Then, the KBr solution and $Bi(NO_3)_3·5H_2O$ solution were transferred into a 50 ml Teflon-lined autoclave and kept at 160°C for 16 h. After cooling down, the precipitate was washed and dried to obtain $Bi_4O_5Br_2$.

The UiO-66/$Bi_4O_5Br_2$ composites were prepared by an electronic assembly technique. Typically, 50 mg $Bi_4O_5Br_2$ with a positive zeta potential of 35.9 mV (**Supplementary Figure S1**) and different amounts of UiO-66 with a negative zeta potential of −20.1 mV (**Supplementary Figure S1**) were dispersed into 50 ml deionized water, respectively, and the above two solutions were mixed together and then sonicated for 60 min to prepare the UiO-66@$Bi_4O_5Br_2$ composite. The adding amount of the UiO-66@ was 5, 10, 15 mg, respectively, and the corresponding UiO-66@$Bi_4O_5Br_2$ samples were named U@B-5, U@B-10, and U@B-15, respectively.

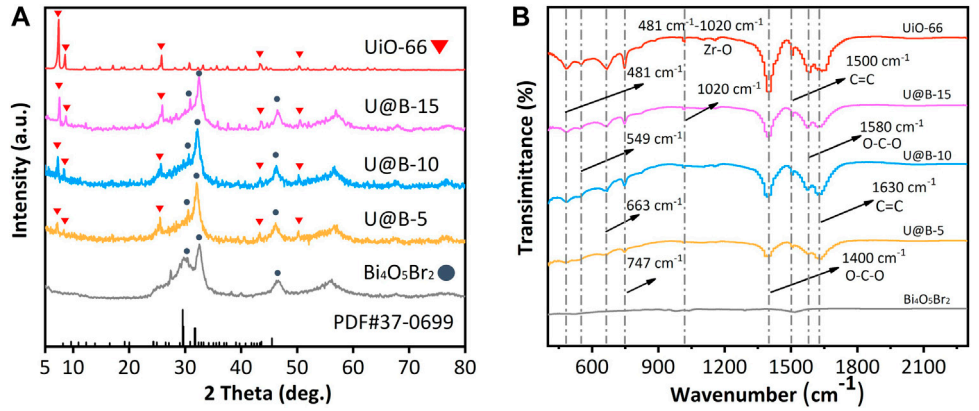

FIGURE 1 | (A) XRD patterns of UiO-66, $Bi_4O_5Br_2$ and U@B-X, **(B)** FTIR spectra of UiO-66, $Bi_4O_5Br_2$, and U@B-X.

2.2 Characterization Techniques

The structure, morphology, composition, and zeta potential were tested using powder X-ray diffraction (XRD, D/Max-2550, Rigaku), field emission scanning electron microscopy (FE-SEM, JXA-840A, JEOL), high-resolution transmission electron microscopy (HR-TEM, JEM-100CX II, JEOL), X-ray photoelectron spectroscopy (XPS, PHI ESCA-5000C, Perkin Elmer), and a ZS90 (Malvern Panalytical) zeta sizer, respectively. The light adsorption, Fourier transform infrared spectrum (FT-IR), Raman spectrum and transient fluorescence absorption spectroscopy were studied by the UV–vis diffuse reflectance spectra (DRS, UV2550 spectrophotometer), Nexus 870 spectrometer, DXR spectrometer, and femtosecond transient absorption spectrometer (Helios fire, Ultrafast System), respectively. The S_{BET} and pore size distribution of the powders were measured on an ASAP 2020 HD88 (United States). The photocurrents, electrochemical impedance spectroscopy (EIS) profiles, and Mott–Schottky plots were tested via a CHI660B electrochemical workstation.

2.3 Photocatalytic Performance Measurements

The photocatalytic CO_2 reduction experiments were measured in an enclosed quartz reactor under Xe lamp irradiation (Perfectlight, PLS-SXE300+) and the reaction temperature was controlled at 5°C by HJDC-0506 instrument to prevent thermal catalytic effects. Typically, 30 mg of U@B-X sample was dispersed in 50 ml of deionized water with no sacrificial agent by stirring for 10 min and then transformed into the enclosed quartz reactor. Then, the reaction container was filled with high purity CO_2 gas (99.995%) and the gaseous products were tested by the GC-2014C gas chromatography (GC, Shimadzu Technologies) equipped with a thermal conductivity detector (TCD) and two flame ionization detectors (FIDs) for the analysis of CO. For the stability measurement, the reactor was re-filled with CO_2 (80Kpa) and then tested under the same condition described above.

2.4 Photoelectrochemical Measurements

The photocurrents, electrochemical impedance spectroscopy (EIS) profiles, Mott–Schottky plots, and Linear sweep voltammetry (LSV) were tested *via* a CHI-760E electrochemical workstation.

Photocurrent measurements of samples were carried out using a three electrodes electrochemical workstation with Ag/AgCl as reference electrode, Pt wire as the counter electrode, and the catalysts as the working electrode using a 75 W 365 nm LED lamp as the light source. The working electrode was prepared with 5 mg catalysts, 250 μL ethanol, 250 μL ethylene glycol, and 40 μL Nafion solution (5 wt%) dip-coated on the FTO conducting glass. Mott-Schottky plot of UiO-66 and $Bi_4O_5Br_2$ were measured without light irradiation at 200 Hz, 400Hz, and 600 Hz frequencies. EIS measurements were tested in the frequency range of 1,000 kHz–0.01 Hz at 0.8 V. LSV measurements were performed by sweeping the potential from 0 to 1.2 V Na_2SO_4 aqueous solution (0.1 M, pH = ca. 7) was used as the supporting electrolyte.

3 RESULTS AND DISCUSSIONS

The composition of different samples was characterized by XRD. Pure $Bi_4O_5Br_2$ shows a series of diffraction peaks at 24.4, 27.4, 29.6, 32.6, and 46.2°, corresponding to (31-1), (212), (11-3), (020), and (422) planes of the standard monoclinic $Bi_4O_5Br_2$ (PDF #37-0699); while the diffraction peaks of UiO-66 are consistent with that reported in the literature (**Figure 1A**) (Dong et al., 2015), indicating the successful synthesis of $Bi_4O_5Br_2$ and UiO-66. Both peaks corresponding to the $Bi_4O_5Br_2$ and UiO-66 are observed in $Bi_4O_5Br_2$/UiO-66 hybrid, no obvious change is observed in the crystal structure after the combination of UiO-66 and $Bi_4O_5Br_2$, indicating successful fabrication of the $Bi_4O_5Br_2$/UiO-66 hybrid (**Figure 1A**). The peak intensity of UiO-66 in the $Bi_4O_5Br_2$/UiO-66 hybrid increases when UiO-66 content increases. The different functional groups of the UiO-66 and the $Bi_4O_5Br_2$/UiO-

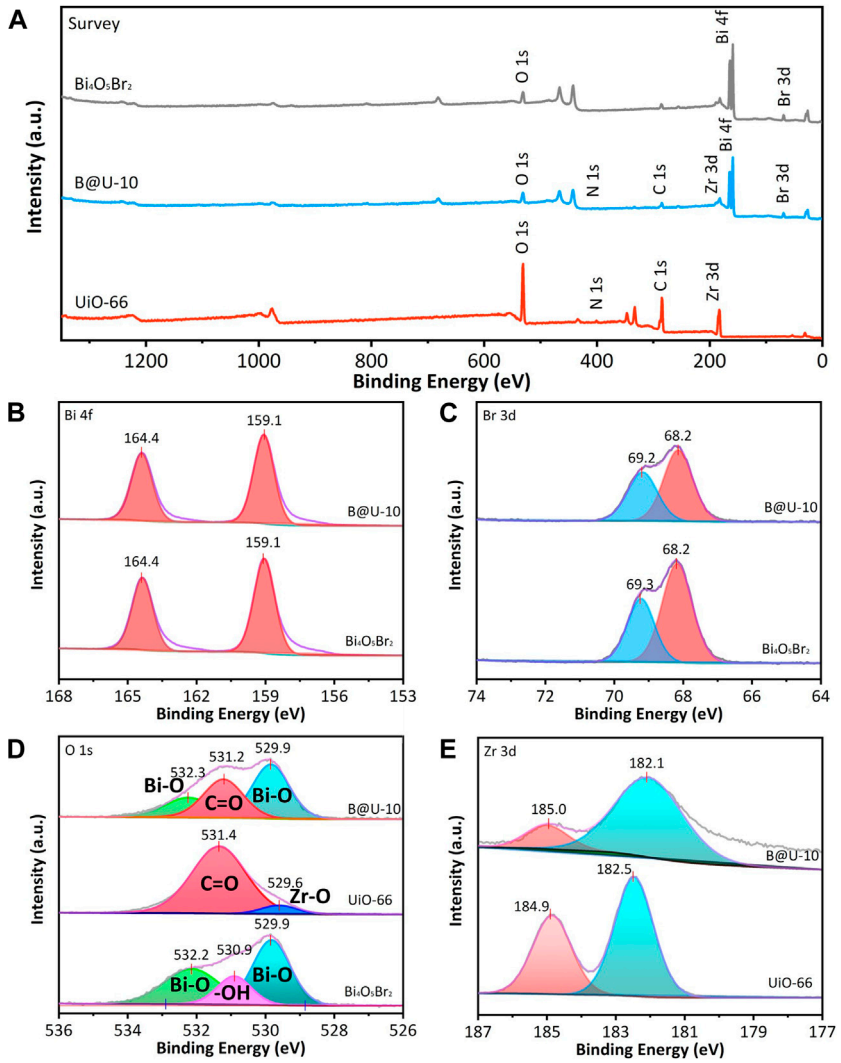

FIGURE 2 | XPS survey spectra **(A)**, high-resolution spectra of **(B)** Bi 4f, **(C)** O 1s, **(D)** Br 3d, and **(E)** Zr 3d for UiO-66, $Bi_4O_5Br_2$, and U@B-10.

66 hybrid were studied via FTIR technique (**Figure 1B**). For pure UiO-66, a series of peaks representing asymmetrical stretching of Zr-(OC) and different bending vibration modes from ligands are observed between 400 and 1,020 cm^{-1} (Bargozideh et al., 2020). The two peaks at 1,400 and 1,580 cm^{-1} represent the O-C-O symmetric and asymmetric tensile vibrations of the carboxyl groups of the ligands of the terephthalic acid part. The peaks at 1,500 and 1,630 cm^{-1} are attributed to the C=C vibration mode of the H_2BDC ligands (Ahmadipouya et al., 2021). The weak peak of C=C for the $Bi_4O_5Br_2$ sample is caused by the adsorption of carbon impurities (glycerin) on the surface during the synthetic process. The $Bi_4O_5Br_2$/UiO-66 hybrids demonstrate almost the same spectra as that of pure UiO-66, indicating that the coupling UiO-66 to $Bi_4O_5Br_2$ would not change the functional group structure of UiO-66. In addition, **Supplementary Figure S2** shows the Raman spectra of UiO-66, $Bi_4O_5Br_2$, and $Bi_4O_5Br_2$/UiO-66 composite. For the UiO-66, the peaks at 1,610, 1,440, and 1,420 cm^{-1} correspond to the C=C stretching and coordination of Zr(IV) ions with the O-C-O symmetric stretching, respectively, while the low-frequency bands at 1,140 and 860 cm^{-1} can be assigned to the deformation band of the benzoic acid group (Bariki et al., 2020). For the $Bi_4O_5Br_2$, two Raman peaks of A_{1g} internal and E_{1g} internal Bi-Br stretching modes are found at 108 and 156 cm^{-1}, respectively (Xu et al., 2021). Both Raman bands belonging to UiO-66 and $Bi_4O_5Br_2$ are observed in the U@B-X composites. The XRD, FTIR, and Raman results further proved the successfully synthesized of $Bi_4O_5Br_2$/UiO-66 hybrids.

The survey XPS spectra show that the $Bi_4O_5Br_2$/UiO-66 composite mainly contains O, C, Zr, Bi, and Br elements (**Figure 2A**), indicating the UiO-66 and $Bi_4O_5Br_2$ are successfully integrated *via* the self-assembly method. The high-resolution spectrum of Bi 4f of the $Bi_4O_5Br_2$ illustrates doublet peaks representing Bi 4f7/2 (159.1 eV) and Bi 4f5/2 (164.4 eV),

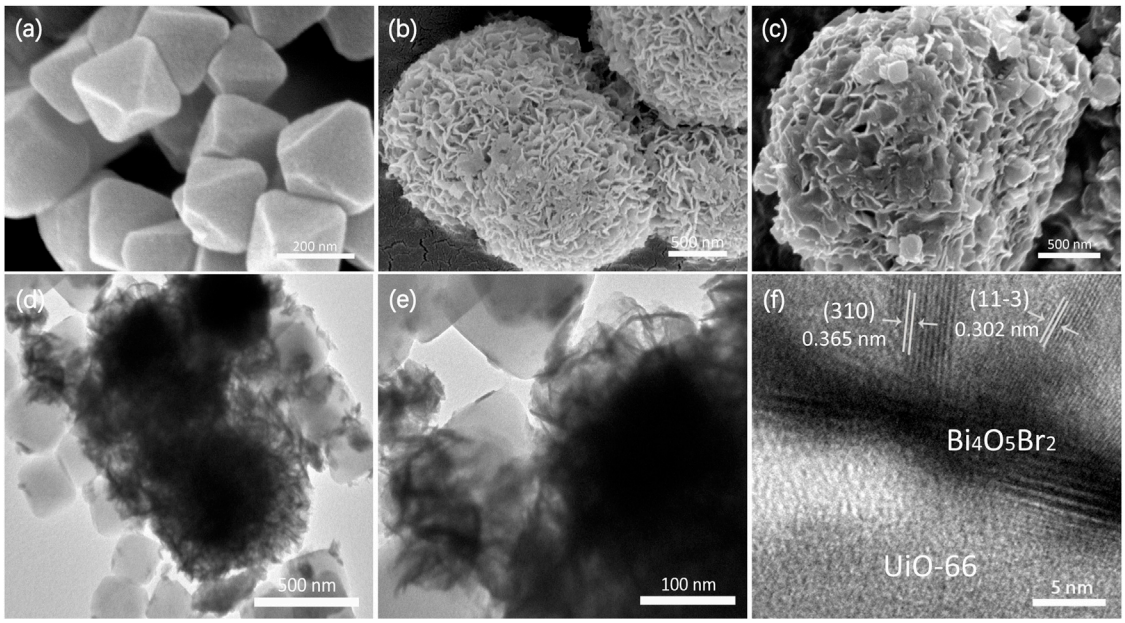

FIGURE 3 | FESEM images of **(A)** UiO-66, **(B)** $Bi_4O_5Br_2$, **(C)** U@B-10, **(D–E)** TEM of U@B-10, and **(F)** HRTEM of U@B-10.

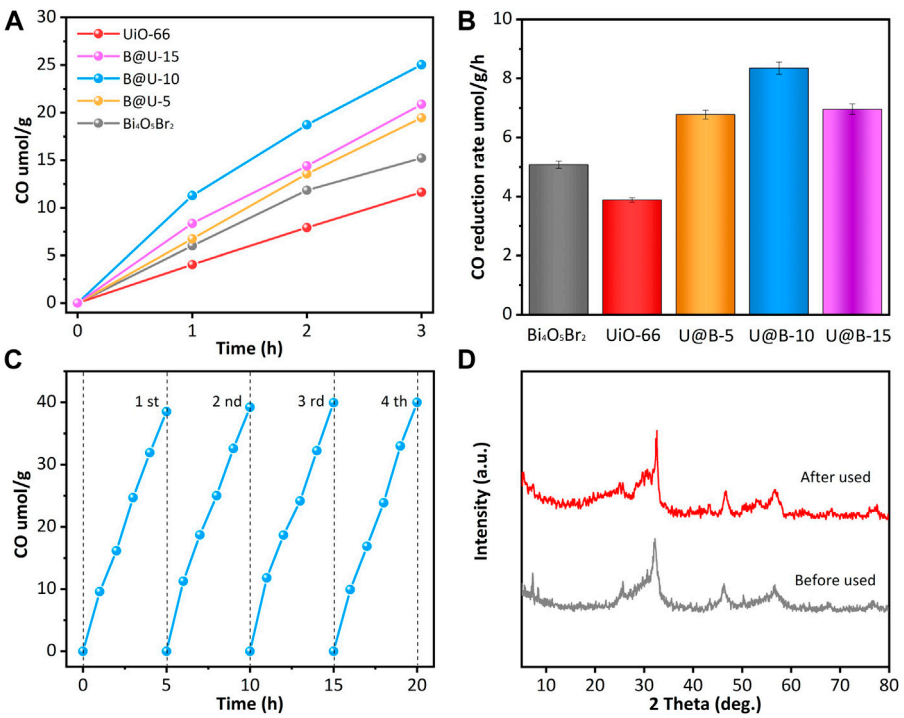

FIGURE 4 | (A) Photocatalytic CO_2 reduction and **(B)** CO_2 reduction rates of different samples; **(C)** stability test of U@B-10 and **(D)** the XRD patterns of U@B-10 before and after cycles.

respectively, implying that Bi atoms are Bi^{3+} in pure $Bi_4O_5Br_2$ (**Figure 2B**) (Ye et al., 2016). For the Bi 4f in U@B-10 composite (**Figure 2B**), the Bi 4f spectrum also can be divided into two peaks at 159.1 and 164.4 eV, and no difference is observed compared to the pure $Bi_4O_5Br_2$, indicating that Bi^{3+} can be maintained. The Br 3d spectrum of $Bi_4O_5Br_2$ can be divided into two peaks at 68.2

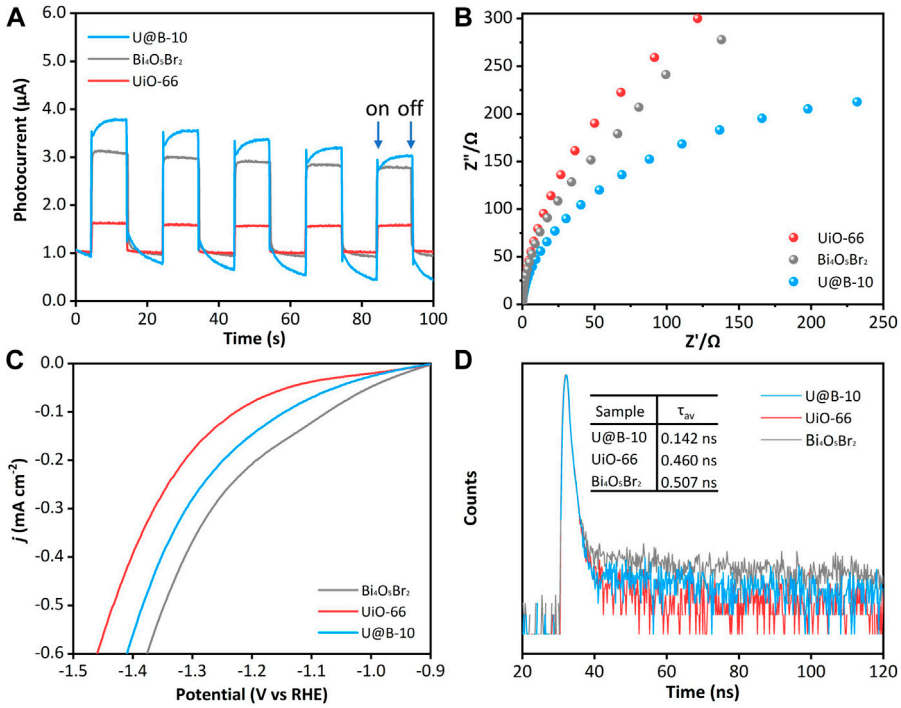

FIGURE 5 | (A) Transient photocurrent spectra, **(B)** EIS spectra, **(C)** LSV curves, **(D)** TRPL of $Bi_4O_5Br_2$, and U@B-10.

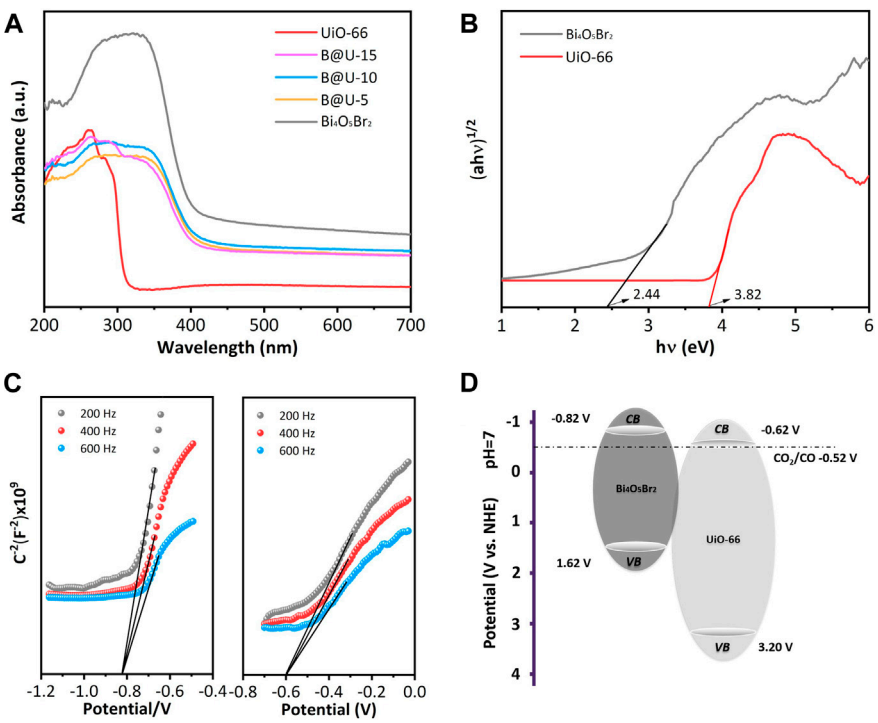

FIGURE 6 | (A) UV–vis spectra, **(B)** Tauc plots, **(C)** MS plots, **(D)** band diagrams of UiO-66, and $Bi_4O_5Br_2$.

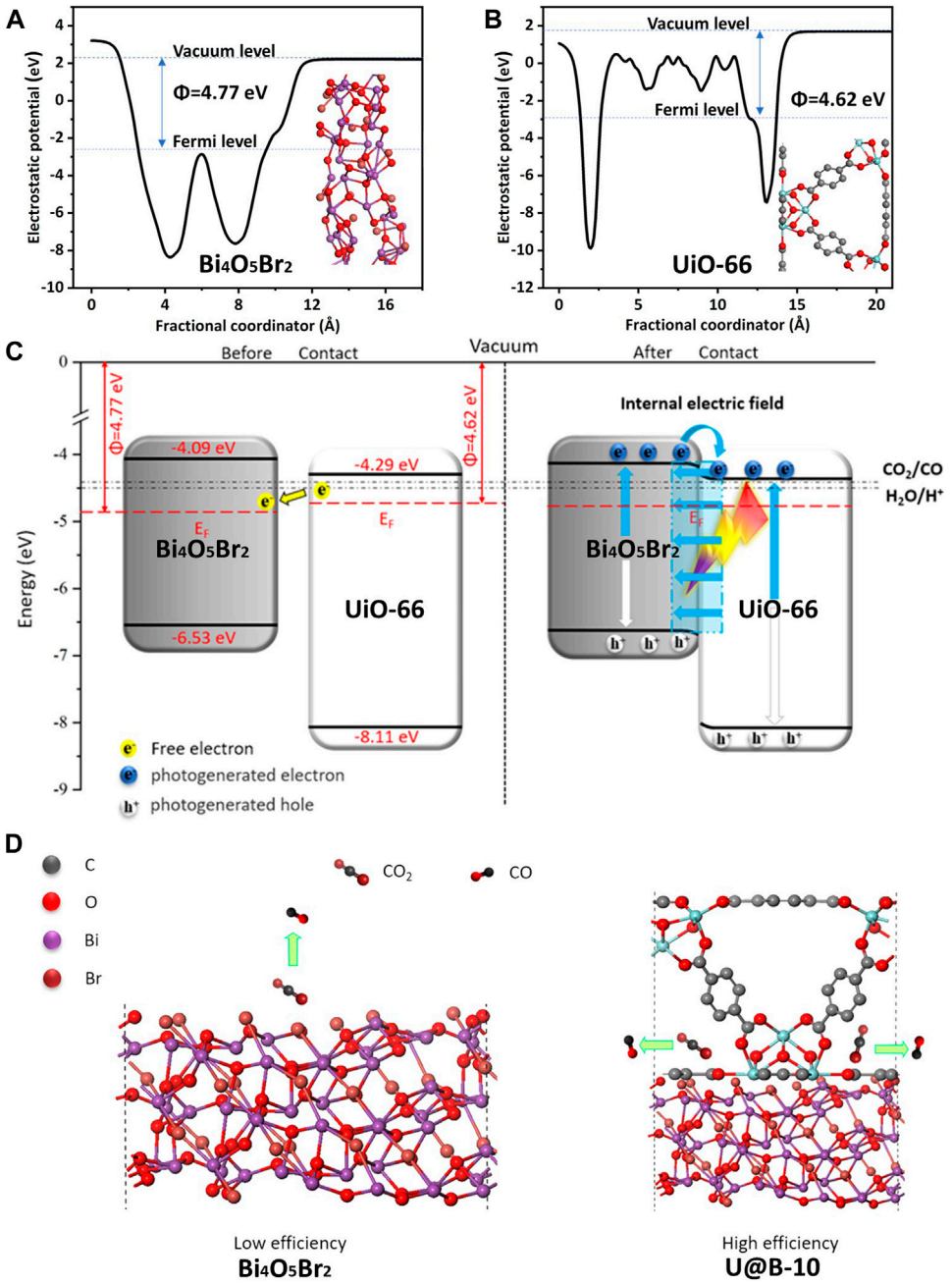

FIGURE 7 | The calculated work functions **(A)** (11-3) plane of $Bi_4O_5Br_2$ and **(B)** (100) plane of UiO-66; **(C,D)** the proposed photocatalytic mechanism of UiO-66/$Bi_4O_5Br_2$ composite.

and 69.3 eV, representing Br 3d5/2 and Br 3d3/2, respectively (**Figure 2C**) (Bai et al., 2019). Besides, the peak position of Br 3d in U@B-10 is still located at 68.2 and 69.2 eV, respectively, revealing the same status of the Br in U@B-10 and $Bi_4O_5Br_2$. The O1s spectrum of UiO-66 in **Figure 2D** is decomposed into two peaks of Zr-O (529.6 eV) and C=O groups (531.4 eV), respectively (Cao et al., 2021). The peaks at 529.9 and 532.2 eV in $Bi_4O_5Br_2$ can be ascribed to the Bi-O band, while the peak of 530.9 eV stands for the surface hydroxyl groups (Chen et al., 2021; Hong et al., 2020). **Figure 2E** shows the spectra of Zr 3d, two strong peaks can be observed at 182.5 and 184.9 eV of UiO-66, corresponding to the Zr 3d5/2, and Zr 3d3/2, respectively (Ding et al., 2017). The XPS results evidenced the successful preparation of the $Bi_4O_5Br_2$/UiO-66 composite.

The SEM image of UiO-66 is illustrated in **Figure 3A**, exhibiting a relatively uniform octahedral prism morphology with an average size of 200 nm. The pure $Bi_4O_5Br_2$ shows

hierarchical and stereoscopic flower morphology, which is made up of small nanosheets (**Figure 3B**). For the U@B-10 hybrid, the UiO-66 octahedral prism is wrapped over the $Bi_4O_5Br_2$ stereoscopic flowers (**Figures 3C,D**). The corresponding energy-dispersive X-ray spectroscopy (EDX) element analysis (**Supplementary Figure S3**) displays the coexistence of Bi, Br, O, and Zr elements at the selected area of U@B-10, further proving the effective hybridization of UiO-66 and $Bi_4O_5Br_2$. Furthermore, an intimate interface and the crystal boundary can be observed between the UiO-66 and $Bi_4O_5Br_2$ (**Figures 3E,F**), which also proves the formation of a heterostructure. **Figure 3F** clearly shows the polycrystalline properties of $Bi_4O_5Br_2$, and the (11-3) and (310) lattice planes of $Bi_4O_5Br_2$ with lattice edges of 0.30 and 0.36 nm, respectively, are also observed in the U@B-10 hybrid. The Brunner–Emmet–Teller (BET) surface area of UiO-66, $Bi_4O_5Br_2$, and U@B-10 composite is displayed in **Supplementary Table S1**, and the U@B-10 composite displays a much larger BET surface area (211.12 $m^2\,g^{-1}$) and pore volume (0.14 $m^3\,g^{-1}$) than that of $Bi_4O_5Br_2$. From the TEM images of the samples can find that part of the surface of UiO-66 was covered by $Bi_4O_5Br_2$ after combination, which decreased the surface area of the composite. The U@B-10 sample owns the highest average pore size (5.92 nm), which is beneficial for exposing more active sites thereby enhancing the photocatalytic activity.

The photocatalytic CO_2 reduction performances were investigated (**Figures 4A,B**). Pure UiO-66 and $Bi_4O_5Br_2$ show rather low CO_2 reduction performance. Pure UiO-66 and $Bi_4O_5Br_2$ present the photocatalytic CO production rate of 3.88 $umolg^{-1}h^{-1}$ and 5.08 $umolg^{-1}\,h^{-1}$, respectively. Compared with pure $Bi_4O_5Br_2$ and UiO-66, coupling the UiO-66 octahedron on $Bi_4O_5Br_2$ can effectively improve the CO_2 reduction efficiency. U@B-X samples demonstrate enhanced CO_2 reduction performance: the photocatalytic CO reduction rate increases in the following order UiO-66 < $Bi_4O_5Br_2$ < U@B-5 < U@B-15 < U@B-10. The low CO_2 reduction of the U@B-15 may be due to the excessive deposition of UiO-66 on $Bi_4O_5Br_2$ impeding the light absorption of $Bi_4O_5Br_2$, thus inhibiting the generation of photogenerated carriers and reducing the transport of carriers. The optimal U@B-10 showed the strongest CO_2 reduction rate of 8.35 $umolg^{-1}h^{-1}$, which is 2.15 times of pure UiO-66 and 1.64 times of pure $Bi_4O_5Br_2$. It is noted that the activity of the U@B-10 is among the best reports for photocatalytic CO_2 reduction (**Supplementary Table S2**). The stability is an important factor in the practical application of high-efficiency photocatalyst, therefore, CO_2 reduction of U@B-10 was carried out four times under the full spectrum light (**Figure 4C**), and the CO production was calculated every 5 h. It can be seen that the CO production remained stable after every cycle and the crystalline structure preserved its original state (**Figure 4D**). All the results above indicate that the sample had excellent stability.

The charge separation behavior was investigated to explore the reason for the enhanced photocatalytic CO_2 reduction performance. **Figure 5A** displays that the intensity of transient photocurrent of the UiO-66 is very low, while the U@B-10 composite demonstrates the highest transient photocurrent density compared to that of the UiO-66 and $Bi_4O_5Br_2$, indicating that the U@B-10 composite owns the fastest separation efficiency of photogenerated carriers (Liu et al., 2020b; Liu et al., 2020c). The EIS was also used to characterize the interface charge carrier transport capacity. As shown in **Figure 5B**, the EIS radius of the U@B-10 composite is smaller than that of pure $Bi_4O_5Br_2$ and UiO-66, indicating that U@B-10 composite presents lower charge transfer resistance and higher separation rate (Liu et al., 2020d; Wang et al., 2020). Furthermore, according to the linear sweep voltammetry (LSV) analysis (**Figure 5C**), U@B-10 shows a lower overpotential and Tafel slope (**Supplementary Figure S4**) than that of pure UiO-66, indicating that the introduction of $Bi_4O_5Br_2$ can decrease the overpotential and promote CO_2 reduction (Liu et al., 2016; Peng et al., 2021). Time-resolved PL spectra were performed (**Figure 5D**). The average lifetime of U@B-10 is shorter (0.142 ns) compared with $Bi_4O_5Br_2$ (0.507 ns) and UiO-66 (0.460 ns), indicating that the U@B-10 heterojunction demonstrates faster transmission speed of the photogenerated carriers (Tang et al., 2019).

Figure 6A reveals the UV-Vis spectra of the UiO-66, $Bi_4O_5Br_2$, and U@B-X composites. Due to the $Zr\text{-}_{OXO}$ cluster and the charge transfer transition between the ligand and Zr (IV) (Yu et al., 2020), UiO-66 exhibits a typical absorption edge at 345 nm (Wang et al., 2016). The $Bi_4O_5Br_2$ demonstrates an obvious absorption edge at 440 nm. The band gap energies of UiO-66 and $Bi_4O_5Br_2$ are calculated to be 3.82 and 2.44 eV, respectively (**Figure 6B**). According to the Mott-Schottky (MS) diagram (**Figure 6C**), the conduction band positions of the UiO-66 and $Bi_4O_5Br_2$ are slated to be −0.62 and −0.82 V, respectively (**Figure 6D**) (Chai et al., 2018; Wei et al., 2021).

Moreover, the work function, which can reveal electron transfer in the heterostructure, was also calculated using the density functional theory (DFT) calculation (Liu et al., 2021b). **Figures 7A,B** shows that the work functions of $Bi_4O_5Br_2$ (11-3) and UiO-66 (100) are 4.09 and 4.29 eV, respectively, indicating that the $Bi_4O_5Br_2$ (11-3) surface Fermi levels is lower than that of UiO-66 (100) surface. Based on the Mott-Schottky curve, $Bi_4O_5Br_2$, and UiO-66 are n-type semiconductors, and their Fermi energy levels are close to the conduction band. Since the Fermi energy level of $Bi_4O_5Br_2$ is lower than that of UiO-66, the electrons of UiO-66 will transfer to $Bi_4O_5Br_2$ until their Fermi energy levels reach equilibrium, and a built-in electric field is formed (Wang et al., 2018b; Tao et al., 2021). Accordingly, a preliminary charge transfer mechanism of U@B-X photocatalyst is proposed (**Figures 7C,D**). The UiO-66 and $Bi_4O_5Br_2$ have a good matching band structure to form a type-II heterojunction. Based on the work functions of $Bi_4O_5Br_2$ (11-3) and UiO-66 (100), the electrons tend to migrate from UiO-66 to $Bi_4O_5Br_2$ forming an internal electric field. Driven by the internal electric field, the photogenerated electrons on the CB of $Bi_4O_5Br_2$ are more easily transferred to the CB of UiO-66 to participate in the CO_2 reduction reaction while the holes on the VB of UiO-66 transferred to the VB of $Bi_4O_5Br_2$ (Wei et al., 2018; Kuang et al., 2021).

4 CONCLUSION

In summary, a series of UiO-66@$Bi_4O_5Br_2$ photocatalysts were prepared via assembling UiO-66 octahedral on $Bi_4O_5Br_2$ nanoflower using a simple electrostatic self-assembly method. The UiO-66@$Bi_4O_5Br_2$ hybrids exhibited elevated photocatalytic CO_2 reduction activity under full-spectrum light illumination without any sacrificial agent, the optimal sample (U@B-10 hybrid) showed the highest CO conversion rate of 8.35 μmol h^{-1} g^{-1}, which was 1.64 and 2.15 times higher than pure $Bi_4O_5Br_2$ and UiO-66, respectively. A possible mechanism of enhanced activity was supposed that UiO-66 and $Bi_4O_5Br_2$ demonstrated well-matched energy band structures and an intimate interface, leading to the construction of a type-II heterojunction with boosted charge separation efficiency and promoted CO_2 reduction activity. This work reports the design of photocatalysts with matched band gap structure and an intimate interface is an effective strategy to realize highly efficient CO_2 reduction.

DATA AVAILABILITY STATEMENT

The datasets presented in this study can be found in online repositories. The names of the repository/repositories and accession number(s) can be found in the article/**Supplementary Material**.

AUTHOR CONTRIBUTIONS

HT and QL conceived and designed the experiments and revised the paper. DL, BZ, and LW performed most of the experiments. ZS performed the DFT calculations. The article was written through contributions of all authors. All authors have given approval to the final version of the article.

FUNDING

This work is sponsored by the National Natural Science Foundation of China (21975110 and 21972058) and HT also appreciates the support from the Taishan Youth Scholar Program of Shandong Province.

SUPPLEMENTARY MATERIAL

The Supplementary Material for this article can be found online at: https://www.frontiersin.org/articles/10.3389/fchem.2021.804204/full#supplementary-material

REFERENCES

Ahmadipouya, S., Heidarian Haris, M., Ahmadijokani, F., Jarahiyan, A., Molavi, H., Matloubi Moghaddam, F., et al. (2021). Magnetic Fe3O4@UiO-66 Nanocomposite for Rapid Adsorption of Organic Dyes from Aqueous Solution. *J. Mol. Liquids* 322, 114910. doi:10.1016/j.molliq.2020.114910

Bai, Y., Yang, P., Wang, L., Yang, B., Xie, H., Zhou, Y., et al. (2019). Ultrathin Bi4O5Br2 Nanosheets for Selective Photocatalytic CO2 Conversion into CO. *Chem. Eng. J.* 360, 473–482. doi:10.1016/j.cej.2018.12.008

Bargozideh, S., Tasviri, M., Shekarabi, S., and Daneshgar, H. (2020). Magnetic BiFeO3 Decorated UiO-66 as a P-N Heterojunction Photocatalyst for Simultaneous Degradation of a Binary Mixture of Anionic and Cationic Dyes. *New J. Chem.* 44, 13083–13092. doi:10.1039/d0nj02594a

Bariki, R., Majhi, D., Das, K., Behera, A., and Mishra, B. G. (2020). Facile Synthesis and Photocatalytic Efficacy of UiO-66/CdIn2S4 Nanocomposites with Flowerlike 3D-Microspheres towards Aqueous Phase Decontamination of Triclosan and H2 Evolution. *Appl. Catal. B: Environ.* 270, 118882. doi:10.1016/j.apcatb.2020.118882

Cao, W., Jiang, C., Chen, C., Zhou, H., and Wang, Y. (2021). A Novel Z-Scheme CdS/Bi4O5Br2 Heterostructure with Mechanism Analysis: Enhanced Photocatalytic Performance. *J. Alloys Compd.* 861, 158554. doi:10.1016/j.jallcom.2020.158554

Chai, Y.-Y., Qu, D.-P., Ma, D.-K., Chen, W., and Huang, S. (2018). Carbon Quantum dots/Zn2+ Ions Doped-CdS Nanowires with Enhanced Photocatalytic Activity for Reduction of 4-nitroaniline to P-Phenylenediamine. *Appl. Surf. Sci.* 450, 1–8. doi:10.1016/j.apsusc.2018.04.121

Chen, Z., Zhao, J., Chen, J., Zhang, Y., Chen, D., Wang, Q., et al. (2021). UiO-66/BiOBr Heterojunction Functionalized Cotton Fabrics as Flexible Photocatalyst for Visible-Light Driven Degradation of Dyes and Cr(VI). *Sep. Purif. Technol.* 258, 118007. doi:10.1016/j.seppur.2020.118007

Ding, J., Yang, Z., He, C., Tong, X., Li, Y., Niu, X., et al. (2017). UiO-66(Zr) Coupled with Bi 2 MoO 6 as Photocatalyst for Visible-Light Promoted Dye Degradation. *J. Colloid Interf. Sci.* 497, 126–133. doi:10.1016/j.jcis.2017.02.060

Dong, D., Yan, C., Huang, J., Lu, N., Wu, P., Wang, J., et al. (2019). An Electron-Donating Strategy to Guide the Construction of MOF Photocatalysts toward Co-catalyst-free Highly Efficient Photocatalytic H2 Evolution. *J. Mater. Chem. A.* 7, 24180–24185. doi:10.1039/c9ta06141j

Dong, W., Feng, C., Zhang, L., Shang, N., Gao, S., Wang, C., et al. (2015). Pd@UiO-66: An Efficient Catalyst for Suzuki-Miyaura Coupling Reaction at Mild Condition. *Catal. Lett.* 146, 117–125. doi:10.1007/s10562-015-1659-4

Hirakawa, H., Shiota, S., Shiraishi, Y., Sakamoto, H., Ichikawa, S., and Hirai, T. (2016). Au Nanoparticles Supported on BiVO4: Effective Inorganic Photocatalysts for H2O2 Production from Water and O2 under Visible Light. *ACS Catal.* 6, 4976–4982. doi:10.1021/acscatal.6b01187

Hong, L., Liu, F., Zang, N., Jin, W., and Yang, C. (2020). Morphology-controllable Formation of MOF-Derived C/ZrO2@1T-2H MoS2 Heterostructure for Improved Electrocatalytic Hydrogen Evolution. *Int. J. Hydrogen Energ.* 45, 14831–14840. doi:10.1016/j.ijhydene.2020.03.184

Jin, X., Lv, C., Zhou, X., Xie, H., Sun, S., Liu, Y., et al. (2019). A Bismuth Rich Hollow Bi4O5Br2 Photocatalyst Enables Dramatic CO2 Reduction Activity. *Nano Energy* 64, 103955. doi:10.1016/j.nanoen.2019.103955

Kim, S.-N., Lee, Y.-R., Hong, S.-H., Jang, M.-S., and Ahn, W.-S. (2015). Pilot-scale Synthesis of a Zirconium-Benzenedicarboxylate UiO-66 for CO2 Adsorption and Catalysis. *Catal. Today* 245, 54–60. doi:10.1016/j.cattod.2014.05.041

Kuang, P., Wang, Y., Zhu, B., Xia, F., Tung, C. W., Wu, J., et al. (2021). Pt Single Atoms Supported on N-Doped Mesoporous Hollow Carbon Spheres with Enhanced Electrocatalytic H 2 -Evolution Activity. *Adv. Mater.* 33, 2008599. doi:10.1002/adma.202008599

Ling, C., Niu, X., Li, Q., Du, A., and Wang, J. (2018). Metal-Free Single Atom Catalyst for N2 Fixation Driven by Visible Light. *J. Am. Chem. Soc.* 140, 14161–14168. doi:10.1021/jacs.8b07472

Liu, L. (2016). Controllable ZnO Nanorod Arrays@carbon Fibers Composites: Towards Advanced CO2 Photocatalytic Reduction Catalysts. *Ceramics Int.* 42, 12516–12520. doi:10.1016/j.ceramint.2016.04.136

Liu, Q., He, X., Peng, J., Yu, X., Tang, H., and Zhang, J. (2021). Hot-electron-assisted S-Scheme Heterojunction of Tungsten Oxide/graphitic Carbon Nitride for Broad-Spectrum Photocatalytic H2 Generation. *Chin. J. Catal.* 42, 1478–1487. doi:10.1016/s1872-2067(20)63753-6

Liu, Q., He, X., Tao, J., Tang, H., and Liu, Z. Q. (2020). Oxygen Vacancies Induced Plasmonic Effect for Realizing Broad-Spectrum-Driven Photocatalytic H 2 Evolution over an S-Scheme CdS/W 18 O 49 Heterojunction. *ChemNanoMat* 7, 44–49. doi:10.1002/cnma.202000536

Liu, Q., Huang, J., Tang, H., Yu, X., and Shen, J. (2020). Construction 0D TiO2 nanoparticles/2D CoP Nanosheets Heterojunctions for Enhanced Photocatalytic H2 Evolution Activity. *J. Mater. Sci. Technol.* 56, 196–205. doi:10.1016/j.jmst.2020.04.026

Liu, Q., Huang, J., Wang, L., Yu, X., Sun, J., and Tang, H. (2020). Unraveling the Roles of Hot Electrons and Cocatalyst toward Broad Spectrum Photocatalytic H 2 Generation of g-C 3 N 4 Nanotube. *Sol. RRL* 5, 2000504. doi:10.1002/solr.202000504

Liu, X., Zhao, Y., Yang, X., Liu, Q., Yu, X., Li, Y., et al. (2020). Porous Ni5P4 as a Promising Cocatalyst for Boosting the Photocatalytic Hydrogen Evolution Reaction Performance. *Appl. Catal. B: Environ.* 275, 119144. doi:10.1016/j.apcatb.2020.119144

Liu, Y., Li, L., Li, Q., Lin, J., Guo, Z., Zhang, X., et al. (2021). Fluorine Doped Porous boron Nitride for Efficient CO2 Capture and Separation: A DFT Study. *Appl. Surf. Sci.* 556, 149775. doi:10.1016/j.apsusc.2021.149775

Liu, Z. Q., Cheng, H., Li, N., Ma, T. Y., and Su, Y. Z. (2016). ZnCo 2 O 4 Quantum Dots Anchored on Nitrogen-Doped Carbon Nanotubes as Reversible Oxygen Reduction/Evolution Electrocatalysts. *Adv. Mater.* 28 (19), 3777–3784. doi:10.1002/adma.201506197

Mukhopadhyay, S., Shimoni, R., Liberman, I., Ifraemov, R., Rozenberg, I., and Hod, I. (2021). Assembly of a Metal-Organic Framework (MOF) Membrane on a Solid Electrocatalyst: Introducing Molecular-Level Control over Heterogeneous CO 2 Reduction. *Angew. Chem. Int. Ed.* 60, 13423–13429. doi:10.1002/anie.202102320

Peña-Velasco, G., Hinojosa-Reyes, L., Morán-Quintanilla, G. A., Hernández-Ramírez, A., Villanueva-Rodríguez, M., and Guzmán-Mar, J. L. (2021). Synthesis of Heterostructured Catalyst Coupling MOF Derived Fe_2O_3 with TiO_2 for Enhanced Photocatalytic Activity in Anti-inflammatory Drugs Mixture Degradation. *Ceram. Int.* 47, 24632–24640. doi:10.1016/j.ceramint.2021.05.185

Peng, J., Shen, J., Yu, X., Tang, H., and Liu, Q. (2021). Construction of LSPR-Enhanced 0D/2D CdS/MoO3− S-Scheme Heterojunctions for Visible-Light-Driven Photocatalytic H2 Evolution. *Chin. J. Catal.* 42, 87–96. doi:10.1016/s1872-2067(20)63595-1

Peng, X., Ye, L., Ding, Y., Yi, L., Zhang, C., and Wen, Z. (2020). Nanohybrid Photocatalysts with ZnIn2S4 Nanosheets Encapsulated UiO-66 Octahedral Nanoparticles for Visible-Light-Driven Hydrogen Generation. *Appl. Catal. B: Environ.* 260, 118152. doi:10.1016/j.apcatb.2019.118152

Prasad, C., Tang, H., Liu, Q., Bahadur, I., Karlapudi, S., and Jiang, Y. (2020). A Latest Overview on Photocatalytic Application of G-C3n4 Based Nanostructured Materials for Hydrogen Production. *Int. J. Hydrogen Energ.* 45, 337–379. doi:10.1016/j.ijhydene.2019.07.070

Ren, X., Gao, M., Zhang, Y., Zhang, Z., Cao, X., Wang, B., et al. (2020). Photocatalytic Reduction of CO2 on BiOX： Effect of Halogen Element Type and Surface Oxygen Vacancy Mediated Mechanism. *Appl. Catal. B: Environ.* 274, 119063. doi:10.1016/j.apcatb.2020.119063

Scott, V., and Geden, O. (2018). The challenge of Carbon Dioxide Removal for EU Policy-Making. *Nat. Energ.* 3, 350–352. doi:10.1038/s41560-018-0124-1

Shen, J., Shen, J., Zhang, W., Yu, X., Tang, H., Zhang, M., et al. (2019). Built-in Electric Field Induced CeO2/Ti3C2-MXene Schottky-junction for Coupled Photocatalytic Tetracycline Degradation and CO2 Reduction. *Ceramics Int.* 45, 24146–24153. doi:10.1016/j.ceramint.2019.08.123

Su, Y., Zhang, Z., Liu, H., and Wang, Y. (2017). Cd0.2Zn0.8S@UiO-66-NH2 Nanocomposites as Efficient and Stable Visible-Light-Driven Photocatalyst for H2 Evolution and CO2 Reduction. *Appl. Catal. B: Environ.* 200, 448–457. doi:10.1016/j.apcatb.2016.07.032

Tang, H., Wang, R., Zhao, C., Chen, Z., Yang, X., Bukhvalov, D., et al. (2019). Oxamide-modified G-C3n4 Nanostructures: Tailoring Surface Topography for High-Performance Visible Light Photocatalysis. *Chem. Eng. J.* 374, 1064–1075. doi:10.1016/j.cej.2019.06.029

Tang, H., Xia, Z., Chen, R., Liu, Q., and Zhou, T. (2020). Oxygen Doped g-C 3 N 4 with Nitrogen Vacancy for Enhanced Photocatalytic Hydrogen Evolution. *Chem. Asian J.* 15, 3456–3461. doi:10.1002/asia.202000912

Tao, J., Yu, X., Liu, Q., Liu, G., and Tang, H. (2021). Internal Electric Field Induced S-Scheme Heterojunction MoS2/CoAl LDH for Enhanced Photocatalytic Hydrogen Evolution. *J. Colloid Interf. Sci.* 585, 470–479. doi:10.1016/j.jcis.2020.10.028

Wang, A., Zhou, Y., Wang, Z., Chen, M., Sun, L., and Liu, X. (2016). Titanium Incorporated with UiO-66(Zr)-type Metal-Organic Framework (MOF) for Photocatalytic Application. *RSC Adv.* 6, 3671–3679. doi:10.1039/c5ra24135a

Wang, J., Chen, J., Wang, P., Hou, J., Wang, C., and Ao, Y. (2018). Robust Photocatalytic Hydrogen Evolution over Amorphous Ruthenium Phosphide Quantum Dots Modified G-C3n4 Nanosheet. *Appl. Catal. B: Environ.* 239, 578–585. doi:10.1016/j.apcatb.2018.08.048

Wang, L., Tan, H., Zhang, L., Cheng, B., and Yu, J. (2021). *In-situ* Growth of Few-Layer Graphene on ZnO with Intimate Interfacial Contact for Enhanced Photocatalytic CO2 Reduction Activity. *Chem. Eng. J.* 411, 128501. doi:10.1016/j.cej.2021.128501

Wang, R., Shen, J., Zhang, W., Liu, Q., Zhang, M., Zulfiqar, et al. (2020). Build-in Electric Field Induced Step-Scheme TiO2/W18O49 Heterojunction for Enhanced Photocatalytic Activity under Visible-Light Irradiation. *Ceramics Int.* 46, 23–30. doi:10.1016/j.ceramint.2019.08.226

Wang, Y., Du, R., Li, Z., Song, H., Chao, Z., Zu, D., et al. (2021). Rationally Designed CdS/Ti3C2 MXene Electrocatalysts for Efficient CO2 Reduction in Aqueous Electrolyte. *Ceramics Int.* 47, 28321–28327. doi:10.1016/j.ceramint.2021.06.249

Wang, Y., Hu, Z., Kundu, T., Cheng, Y., Dong, J., Qian, Y., et al. (2018). Metal-Organic Frameworks with Reduced Hydrophilicity for Postcombustion CO2 Capture from Wet Flue Gas. *ACS Sustain. Chem. Eng.* 6, 11904–11912. doi:10.1021/acssuschemeng.8b02173

Wei, R.-B., Huang, Z.-L., Gu, G.-H., Wang, Z., Zeng, L., Chen, Y., et al. (2018). Dual-cocatalysts Decorated Rimous CdS Spheres Advancing Highly-Efficient Visible-Light Photocatalytic Hydrogen Production. *Appl. Catal. B: Environ.* 231, 101–107. doi:10.1016/j.apcatb.2018.03.014

Wei, S., Heng, Q., Wu, Y., Chen, W., Li, X., and Shangguan, W. (2021). Improved Photocatalytic CO2 Conversion Efficiency on Ag Loaded Porous Ta2O5. *Appl. Surf. Sci.* 563, 150273. doi:10.1016/j.apsusc.2021.150273

Wu, Y. A., McNulty, I., Liu, C., Lau, K. C., Liu, Q., Paulikas, A. P., et al. (2019). Facet-dependent Active Sites of a Single Cu2O Particle Photocatalyst for CO2 Reduction to Methanol. *Nat. Energ.* 4, 957–968. doi:10.1038/s41560-019-0490-3

Xu, M., Wang, Y., Ha, E., Zhang, H., and Li, C. (2021). Reduced Graphene oxide/Bi4O5Br2 Nanocomposite with Synergetic Effects on Improving Adsorption and Photocatalytic Activity for the Degradation of Antibiotics. *Chemosphere* 265, 129013. doi:10.1016/j.chemosphere.2020.129013

Xu, Q., Zhang, L., Cheng, B., Fan, J., and Yu, J. (2020). S-scheme Heterojunction Photocatalyst. *Chem* 6, 1543–1559. doi:10.1016/j.chempr.2020.06.010

Yang, Z., Xu, X., Liang, X., Lei, C., Gao, L., Hao, R., et al. (2017). Fabrication of Ce Doped UiO-66/graphene Nanocomposites with Enhanced Visible Light Driven Photoactivity for Reduction of Nitroaromatic Compounds. *Appl. Surf. Sci.* 420, 276–285. doi:10.1016/j.apsusc.2017.05.158

Ye, L., Jin, X., Liu, C., Ding, C., Xie, H., Chu, K. H., et al. (2016). Thickness-ultrathin and Bismuth-Rich Strategies for BiOBr to Enhance Photoreduction of CO 2 into Solar Fuels. *Appl. Catal. B: Environ.* 187, 281–290. doi:10.1016/j.apcatb.2016.01.044

Yu, H., Ma, H., Wu, X., Wang, X., Fan, J., and Yu, J. (2020). One-Step Realization of Crystallization and Cyano-Group Generation for g-C 3 N 4 Photocatalysts with Improved H 2 Production. *Sol. RRL* 5, 2000372. doi:10.1002/solr.202000372

Zeama, M., Morsy, M., Abdel-Azeim, S., Abdelnaby, M., Alloush, A., and Yamani, Z. (2020). Photophysical and Photocatalytic Properties of Structurally Modified UiO-66. *Inorg. Chim. Acta* 501, 119287. doi:10.1016/j.ica.2019.119287

Zhang, X., Fan, Y., You, E., Li, Z., Dong, Y., Chen, L., et al. (2021). MOF Encapsulated Sub-nm Pd skin/Au Nanoparticles as Antenna-Reactor Plasmonic Catalyst for Light Driven CO2 Hydrogenation. *Nano Energy* 84, 105950. doi:10.1016/j.nanoen.2021.105950

Zhang, X., Song, L., Bi, F., Zhang, D., Wang, Y., and Cui, L. (2020). Catalytic Oxidation of Toluene Using a Facile Synthesized Ag Nanoparticle Supported on UiO-66 Derivative. *J. Colloid Interf. Sci.* 571, 38–47. doi:10.1016/j.jcis.2020.03.031

Conflict of Interest: The reviewer (HY) declared a past co-authorship with one of the authors (HT) to the handling Editor.

Publisher's Note: All claims expressed in this article are solely those of the authors and do not necessarily represent those of their affiliated organizations, or those of the publisher, the editors and the reviewers. Any product that may be evaluated in this article, or claim that may be made by its manufacturer, is not guaranteed or endorsed by the publisher.